Conceptual Design of Propulsors for the SUSAN Electrofan Transport Aircraft

Byung Joon Lee[*] and May-Fun Liou[**]
NASA Glenn Research Center, Cleveland, OH, USA, 44142

Conceptual designs of the propulsor modules for the SUSAN electro-fan aircraft are sought after. Shaft power requirement is reduced by using boundary layer ingesting propulsion technology. There are several obstacles to designing feasible BLI propulsion systems such as inlet distortion, flow blockage from ingesting low-momentum flow, strong coupling between airframe and propulsion systems. Thus, the high fidelity CFD tool is indispensable to assess the performance of the propulsion systems and evaluate the inlet profiles during the design process. Consequently, the CFD data is used to update the inputs for the NPSS model from the initial stage of the system design. Hence, the inlet sizing, fan design, and estimation of the power saving are carried out. Various installation concepts of the mail-slot nacelle, such as under-/over-wing and trailing edge configurations, are investigated for the wing-mounted turbo-electric distributed propulsor module, and their power-saving is evaluated. As for the tail-mounted turbofan engine, the fan diameter and inlet captured area is determined based on the CFD profiles. An appropriate area ratio of the bypass and core ducts is derived from meeting the target bypass ratio from the system design. The baseline fan stage is analyzed by full annulus URANS CFD to assess the efficiency penalty due to the ingested pressure and swirl distortions.

I. Nomenclature

α: flow angularity from absolute frame
β: flow angularity from relative frame
BLI: Boundary Layer Ingestion
γ: specific heat ratio
c: chord length of airfoil
C_p: specific heat capacity at constant pressure
C_u: circumferential component of velocity in the absolute frame
C_z: axial component of velocity in the absolute frame
CRF: Counter-Rotating Fan
D: diffusion factor
DP: design point
DTF: distortion tolerant fan
η: polytropic efficiency
EAP: Electrified Aircraft Propulsion
F_u: turning force
FPR: fan pressure ratio
FSPR: fan stage pressure ratio
HPR: high pressure ratio
HS: high speed
H_T: total enthalpy
IGV: Inlet Guide Vane
LE: Leading Edge
LPR: low pressure ratio
LS: low speed
m: mass
$\dot{m}$: mass flow rate in illustration and equations
MFR: mass flow rate
MFR_c: corrected mass flow rate
N_c: corrected speed
NPSS: National Propulsion System Simulation
OGV: Outlet Guide Vane
Om: angular velocity (=ω)
P_{shft}: shaft power
PAI: Propulsion Airframe Integration
PR: pressure ratio
r: coordinate in radial direction
σ: solidity of blade row (=c/s)
s: circumferential distance (pitch) between neighboring blades
STARC_ABL: Single-aisle Turboelectric AiRcraft with Aft Boundary Layer propulsor
SUSAN: SUbsonic Single Aft eNgine
TCT: Tail-Cone Thruster
TeDP: Turbo-electric Distributed Propulsion
TE: Trailing Edge
TSFC: Thrust Specific Fuel Consumption
T_T: total temperature
T_u: Torque
φ: pressure ratio of a blade row
U: rotational velocity of a rotor
W: circumferential component of velocity in the relative frame
$W_{k,rotor}$: work done by a rotor
ω: angular velocity

[*] Aerospace Engineer, HX5, LLC, Turbo-electric and Turbomachinery Systems Branch, NASA Glenn Research Center
[**] Aerospace Engineer, Inlet and Nozzle Branch, NASA Glenn Research Center

II. Introduction

The Susan electrofan aircraft concept is a subsonic regional jet transport aircraft that utilizes Electrified Aircraft Propulsion (EAP) concept to enable propulsive and aerodynamic benefits to reduce fuel consumption, emissions, and cost. The definition of the conceptual mission and performance requirements can be found in ref. [1]. Electrified Aircraft Propulsion (EAP) has attracted a tremendously increasing interest during the last decade. Even though EAP encompasses a broad range of propulsion architectures, a common feature is that electrical power transmits some or all of the propulsive energy. Electric power can be extracted from various devices such as combustion engines, batteries, fuel cells, et cetera. Meanwhile, the thrust-generating propulsors are placed to maximize the synergistic aerodynamic and propulsion benefits from the airframe. National Aeronautics and Space Administration (NASA) has initiated several EAP projects, including N3-X, Single-aisle Turboelectric AiRcraft with an Aft Boundary-Layer propulsor (STARC-ABL), D8, and others, to face the challenges of environmentally responsible aviation [2]. A paradigm shift to purely electrified propulsion aircraft is yet to be realized because the energy storage for high power density is not mature enough. However, a hybrid-electric propulsion system that extracts power from the combustion engines and generates electricity for the motor-driven propulsors is deemed a realizable goal. SUSAN electro-fan adopts the hybrid-electric propulsion concept and consists of two sub-systems, a turboelectric distributed propulsion (TeDP) [3] system installed on the wing and a tail-mounted turbofan engine. The thrust sharing scheme is that 65% of the total requirement is generated by TeDP and the other 35% by the turbofan engine. The required shaft power is extracted from the core of the tail-mounted engine. The SUSAN conceptual layout is displayed in Fig. 1, and the diagram of the propulsion system is illustrated in Fig. 2. The TeDP system employs multiple small separate mail-slots, and each houses a pair of counter-rotating fans powered by a highly efficient electric power transmission system. The tail-mounted engine combines a traditional gas turbine with a boundary layer ingesting (BLI) concept and is dubbed a tail-cone thruster (TCT). The idea takes advantage of the boundary layer ingestion because of its high propulsive efficiency and reduced wake dissipation of the vehicle [4]. In Figs. 2, the figure on the right-hand side illustrates an example of a TCT with a hydrocarbon burning engine located at the core. The power from the core gas turbine is transmitted to a tail-mounted fan stage mechanically. As a result, SUSAN could reduce the loss due to the conversion between the electrical and mechanical powers for the tail-mounted propulsor. The unique features that differentiate the SUSAN propulsion system from STARC_ABL [5] are that the core ingests the boundary layer flow, and the wing mounted engines are distributed and electrically driven BLI propulsors. Both sub-systems are BLI type propulsion systems so that the performance benefits can be maximized.

There have been various approaches applied to evaluating the benefit of BLI propulsion, from one-dimensional engine cycle model to three-dimensional computational fluid dynamics (CFD), and wind-tunnel tests [6-9]. Felder et al. predict that BLI technology provides STARC-ABL a 3.4% reduction in fuel consumption for a single-aisle class for the design mission of 3500 nm and a 2.7% reduction for a 900 nm mission [6]. Meanwhile, if a more accurate prediction is desired, BLI propulsion needs to be addressed from the perspective of propulsion airframe integration (PAI). A recent CFD study that accounts for the BLI propulsion system through coupling inlet, fan, exit-guide-vanes (EGVs), and nozzle predicts a 4.2–4.5% propulsive efficiency gain over a conventional non-BLI type [8]. However, BLI propulsion also incurs the pressure and swirl distortions at the fan face such that the distortion tolerant turbomachinery technologies are mandated.[9]

Even though the BLI propulsion system has a promising potential for power saving, the redemption of benefit through an appropriate design process is still challenging. Most of all, the interaction between airframe and propulsor is not linear, especially for the tightly coupled configurations. Low fidelity models

without considering those PAI coupling effects can hardly predict the performance metrics correctly during the BLI propulsion system design process. To employ the high-fidelity CFD models as a design tool at the conceptual or preliminary design stage when BLI testing data lacks, a tightly coupled PAI model turns out too computationally expensive and may not be practical for the conceptual design stage. Instead, a hybrid approach by loosely coupling PAI CFD and turbomachinery CFD is applied to incorporate the coupling effect in the current design study.

The paper discusses the approaches and processes in designing SUSAN's BLI propulsors of TCT and TeDP to satisfy the design targets from Chau et al. [10]. Moreover, further power saving from the system design goals are sought after by finding out alternative concepts and quantifying the saving through a high-fidelity CFD assessment. This paper is organized as follows; Section II describes the challenges in designing the TeDP system and compares a single-stage fan-OGV configuration with the proposed counter-rotating fans in terms of the efficiency and operability perspectives. The sizing and components design of the tail mounted TCT are detailed in Sec. III. The assessments of the propulsion-airframe integration are also described in this section and followed by the conclusion in Sec. IV.

Figure 1: A provisional layout of the turboelectric SUSAN electro-fan aircraft at conceptual design stage.

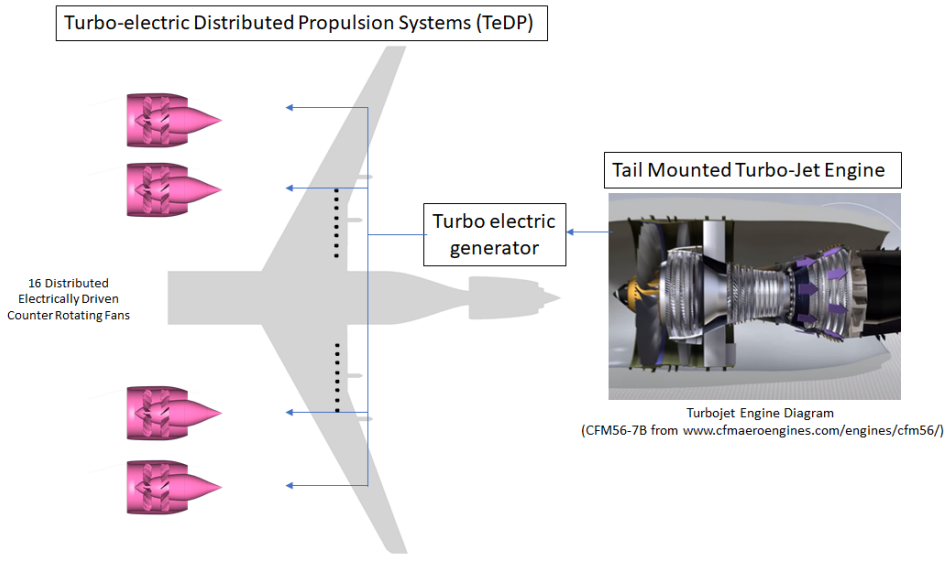

Figure 2: Illustration of the Susan EAP systems; configuration shows a high degree of flexibility.

III. SUSAN-TeDP: mail slot nacelle concept

One of the most significant advantages of the distributed electric propulsion concepts is that the bypass ducts are decoupled from the core and powered by electricity transmission. As a result, the system designer has more flexibility in choosing the concepts and location of the propulsors. SUSAN was initially designed with distributed ducted electric propulsion system installed under the wing, as shown in Fig. 2. The present study addresses the performance aspects of the TeDP systems along with the BLI benefits and the justification of adopting low-speed/low-pressure counter-rotating fans as a part of the efforts to elevate the distortion tolerance of the fan stage. The following sub-chapter discusses the design requirement from the system design [10], the achievement and possible further improvement from reducing TSFC (Thrust Specific Fuel Consumption) by investigating high-fidelity CFD analysis results from the propulsion-airframe model. Then the rest of Sec. II details the employed counter-rotating fans (CRFs) [11] systems, which are designed for Type I distortions [12]. Those discussed include performance assessments of the propulsors in terms of fan map, and evaluations of the power saving with respect to different concepts of the installation of propulsors such as over-wing and or trailing-edge mounted configurations.

Table 1. Design Conditions for the 16 distributed electric propulsors of single-stage fan configuration. [10]

Operating point	Top of climb (ADP)	Takeoff
Thrust [lb]	7,475	36,400
Mach []	0.78	0.2
Altitude [ft]	37,000	0

16 Engines		
FPR	1.25	1.22
Polytropic efficiency []	0.960	0.963
Fan diameter [ft]	2.55	2.55
MFR [kg/s]	33.53	79.19
MFR total [kg/s]	536.48	1267.04
Rotational speed [rpm]	6,395	5,904
Shaft power [MW]	0.5565	1.371
SP total [MW]	8.904	21.942

III.1. Inlet sizing and BLI benefits from wing wake ingestion

The SUSAN-TeDP design employs 16 proposers to reduce the fan diameter and the required shaft power per motor. The design has evolved from the original single-stage transonic fan suggested by the existing database to the current CRFs. Design specifications are given in Table 1, which can also be found in Table 2 of Ref. [10]. As the shape factor of the incoming boundary layer changes, there are significant changes in the operating conditions and the performance of the fan stage depending on the relative size and location of the nacelle concerning the airframe. Thus, these characteristics cannot be analyzed, nor designed by the traditional 0-D, 1-D, and 2-D system design tools, such as meanline code and streamline curvature models [13], because that the inlet profile is 2-dimensional (non-axisymmetric) and keeps changing its shape depending on the geometric dimensions of the nacelle and the airframe. Hence, a high fidelity 3-D CFD PAI model that can predict the inlet profile going into the nacelle and simulate the interactions between the external potential flow field and the suction effect from the operation of the fan stage is essential tool to design the BLI propulsors. [14]

The total thrust generation at the aerodynamic design point (ADP) is needed to be 7475 lbs, 2/3 of the requirement for the whole aircraft system [10]. The under-wing propulsor design is tested on an infinite wing using PAI CFD [15], as shown in Fig. 3. LAVA code [16] is employed in the PAI approach, and LAVA's actuator zone model is used to simulate the first-order effects of the fan in the BLI propulsor. In other words, the actuator zone model imposes pressure rise throughout the zone with either thrust or torque profiles and generates an adequate suction effect on the upstream flow field of the compression zone. The analyses for the inlet profiles on the PAI simulation are carried out at Mach number 0.78 in 37,000 ft altitude conditions. The present study adopted an in-house designed CRFs at Glenn Research Center, and this CRFs system was designed originally for Type-I distortions for an N3-X hybrid wing-body aircraft [11]. The fan stage and flow paths are re-sized to the SUSAN-TeDP scale, and the performance at the ADP condition is assessed by checking whether the thrust output and the mass flow rate meet requirements set by a system designer. The fan stage pressure ratio (FSPR) is set to be 1.25, which can be decomposed into two blade rows, and thus the pressure ratio is about 1.12 per blade row. The mass flow rate per unit is 33.53 kg/sec at the altitude condition and 79.2 kg/sec at the take-off condition at sea level. The maximum shaft power requirement at the take-off condition is 1.37 MW per engine unit and is split into two motors of 0.7 MW level for the counter-rotating fan systems. The rotational speed for the CRFs is 40% lower than the speeds of the single-stage fans as the two fans are sharing the loads. The above advantageous specifications do not reflect the power-saving benefit from the boundary layer ingestion. Therefore, the power savings due to the changes in the present conceptual design studies will be additional gains for the propulsion system.

Figure 3 shows pressure, Mach number, and total pressure contours of an under-wing mounted single unit propulsor (DeP) at FSPR=1.25. They are obtained using LAVA code as the PAI CFD model [15] to extract inlet profiles for the turbomachinery domain. Those inlet profiles are inputs into the turbomachinery model for estimating the propulsive performance of DeP. The decoupled and iterative processes between the PAI CFD model and turbomachinery CFD model are conducted until the design goals are met. Here, the nacelle size is reduced until the thrust generation reaches the target value of 467 lbf (= 2.08kN). At the fourth iteration, the final operating condition that meets the requirement at ADP is presented in table 2. As the BLI propulsion fundamentally reduces the ram drag at the inlet of the nacelle, thus the thrust requirement can be fulfilled with less power than the clean inlet flow engines [14]. The theoretical power saving is obtained from ref [24]. The following subsections will present more detail on CRFs design for the SUSAN-TeDP system.

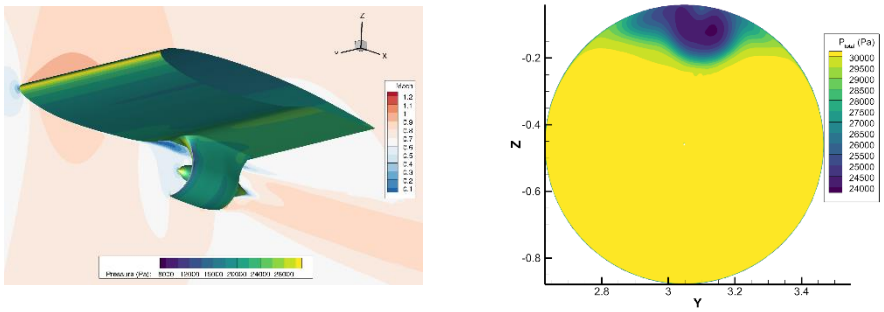

(a) Pressure and Mach number distribution around the Propulsion-Airframe Model [Left]
(b) Total Pressure Profile at the inlet of under-wing configuration (FSPR=1.25)

Figure 3: PAI CFD model for the nacelle sizing and Inlet profile for Turbomachinery CFD model.

Table 2. Operating Conditions for Underwing configuration with Boundary Layer Ingestion.

No. of Engine Units	FSPR	Installation	Fan diameter [ft]	Shape Factor (H)	Iteration No.
	1.25	Under-wing	2.41	1.14	04
16	**MFR [kg/sec]**	**Shaft Pwr [MW]**	**Thrust Generation (kN)**	**Power Saving (%)**	**Theoretical Power Saving (%)**
	30.3	0.49	2.08	12.2	13.5

III.2. Determination of the Operating Conditions for Counter-Rotating Fan stage.

One of the most critical decisions in counter-rotating fan design is finding an optimal splitting of the fan pressure and speed ratios between two rotors. In general, the rear rotor experiences a high diffusion factor. It lacks flow capacity because the inlet relative flow angle (β) is excessively high, as shown in the velocity vector diagram in Fig.3. The second rotor is also constrained by the need to turn the flow swirl angle (α_{goal}) back to near zero degree at the exit to maximize the propulsor's axial momentum. As a result, this low angle constraint at the exit of the counter-rotating fan provides a beneficial correlation of the distribution of the fan pressure ratio between rotors.

The turning force, F_U, in the tangential direction,

$$F_U = \frac{d(mC_U)}{dt} = \dot{m}(dC_U) = \dot{m}(\Delta C_U) = \dot{m}(C_{U2} - C_{U1}) \tag{1}$$

where C_U denotes the circumferential velocity in the absolute frame for stations 1, 2, 3, and 4 corresponding to the LE, TE of the front and rear rotors, respectively. *t* depicts the physical time.

The torque, T_U is,

$$T_U = \frac{d(mrC_U)}{dt} = \dot{m}(d(rC_U)) = \dot{m}(\Delta(rC_U)) = \dot{m}(r_2C_{U2} - r_1C_{U1}), \tag{2}$$

where, *r* represents the radii of each location in the corresponding station and $\dot{m}$ denotes the mass flow rate. Similarly, the shaft power P_{shaft} is

$$P_{shaft} = \dot{m}\omega(r_2C_{U2} - r_1C_{U1}) = \dot{m}(U_2C_{U2} - U_1C_{U1}). \tag{3}$$

And the work done by the front rotor is

$$W_{k_{rotor}} = \omega(r_2C_{U2} - r_1C_{U1}) = r_2\omega_1C_{z2}\tan\alpha_2 - r_1\omega_1C_{z1}\tan\alpha_1 \tag{4}$$

Here, C_z the is axial velocity for each station and α depicts the flow swirl angle at the edges of the blades.

The pressure ratios of the front (φ_1) and rear (φ_2) rotors are,

$$\varphi_1 = \frac{P_{T2}}{P_{T1}} = \left(\frac{T_{T2}}{T_{T1}}\right)^{\frac{\eta_1\gamma}{\gamma-1}} = \left(\frac{H_{T2}}{H_{T1}}\right)^{\frac{\eta_1\gamma}{\gamma-1}} = \left(1 + \frac{U_2C_{U2} - U_1C_{U1}}{C_pT_{T1}}\right)^{\frac{\eta_1\gamma}{\gamma-1}} \tag{5}$$

$$\varphi_2 = \frac{P_{T4}}{P_{T3}} = \left(\frac{T_{T4}}{T_{T3}}\right)^{\frac{\eta_2\gamma}{\gamma-1}} = \left(\frac{H_{T4}}{H_{T3}}\right)^{\frac{\eta_2\gamma}{\gamma-1}} = \left(1 + \frac{U_4C_{U4} + U_3C_{U3}}{C_pT_{T3}}\right)^{\frac{\eta_2\gamma}{\gamma-1}}, \tag{6}$$

where the polytropic efficiency of each rotor is η_1 and η_2, respectively.

Assuming the inlet swirl angle (α_1) being 0°, and no power added into the stream tube contraction between the trailing edge of the front rotor and the leading edge of the rear rotor, i.e.,

$$T_{T3}=T_{T2}, \tag{7}$$

equation (4), (5), and (6) can be further simplified as

$$1+\frac{r_2\omega_1 C_{z2}\tan\alpha_2}{C_pT_{T1}}=\varphi_1^{\frac{\gamma-1}{\eta_1\gamma}},\ \text{and}\quad 1+\frac{r_3\omega_2 C_{z3}\tan\alpha_3}{C_pT_{T3}}=\varphi_2^{\frac{\gamma-1}{\eta_2\gamma}}\ \ (\text{only if } \sin(\alpha_{goal})\cong 0) \tag{8}$$

Consequently, the equations (8) will be re-arranged as,

$$\varphi_2^{\frac{\gamma-1}{\eta_2\gamma}}=1+\omega_2/\omega_1\frac{\kappa(\varphi_1^{\frac{\gamma-1}{\eta_1\gamma}}-1)C_pT_{T1}}{C_pT_{T2}},\ \text{where}\ \kappa=\frac{r_3C_{z3}\tan\alpha_3}{r_2C_{z2}\tan\alpha_2}. \tag{9}$$

Thus, the rotational speed and pressure ratio of the counter-rotating fans can be correlated as follows,

$$\frac{\omega_2}{\omega_1}=\frac{1}{\kappa}\frac{\varphi_2^{(\gamma-1)/(\eta_2\gamma)}-1}{1-\varphi_1^{-(\gamma-1)/(\eta_1\gamma)}}\ . \tag{10}$$

The κ in the equation (10) depends on the contraction of the flow path as in Eq.(11)

$$\kappa=\frac{r_3C_{z3}\tan\alpha_3}{r_2C_{z2}\tan\alpha_2}=\left(\frac{r_{2,s}^2-r_{2,h}^2}{r_{3,s}^2-r_{3,h}^2}\right), \tag{11}$$

The equation (11) is obtained from the conservation equations of the mass and angular momentum. Here, the subscripts *s* and *h* denote shroud and hub at each station. The κ in the present flow path between stations 2 and 3 is 1.153. At four combinations of the efficiency sets, (η_1, η_2), i.e., (0.95, 0.90), (0.90, 0.90), (0.90, 0.83) and (0.96, 0.83), the corresponding speed ratio versus pressure ratio curves for the FSPR=1.25 at the ADP are plotted in Fig. 5.

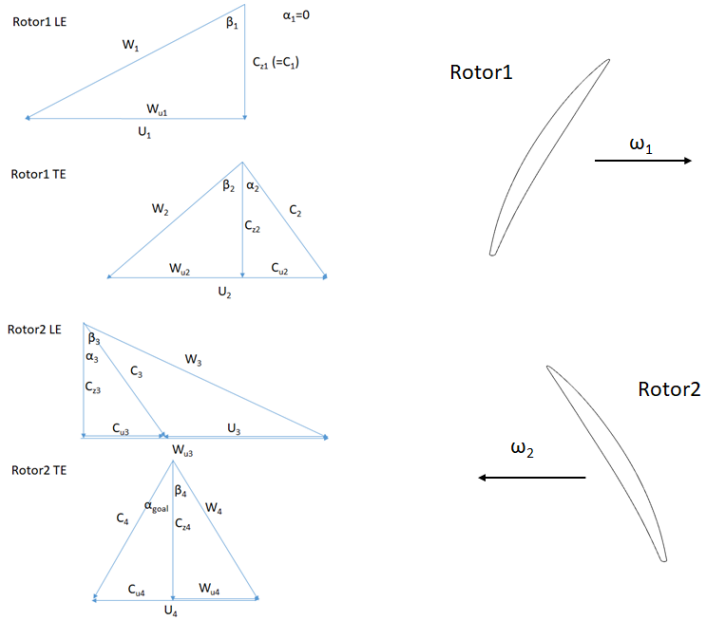

Figure 4: Velocity Vector Diagram for Counter-Rotating Fan System (W: velocity in relative frame)

The most critical concern in designing counter-rotating fans is to match the flow capacity of the two rotors. Thus, excessive hub a conventional fan-OGV system may cause a lack of flow capacity in the 2nd stage. On the other hand, an open flow path will increase the diffusion factor of the stage. Thus, an optimal

pocket of the speed range of the rear rotor could be obtained by the following considerations for the given flow path constraints. The diffusion factor of the rotor can be evaluated by equation (12),

$$D_{R2} = 1 - \frac{W_4}{W_3} + \left|\frac{r_4 C_{U4} - r_3 C_{U3}}{(r_4 + r_3)\sigma W_3}\right| \leq D_{max} (\cong 0.5) \tag{12}$$

and it is subjected to a geometric constraint of D_{max}. [13]

Hence, the pressure ratio of the rear rotor is determined to be 1.12 and the front rotor will raise the pressure by 1.13 times and the speed ratio is determined at 0.94 according to Figure 4. For the current fan diameter 2.41ft (0.734m), the corrected speeds of the front and rear rotors are $N_{c,1}$=5000RPM and $N_{c,2}$=4700RPM respectively. The CFD analyses with the initial speed ratio are performed and checked if the efficiency target could be achieved in the following chapters.

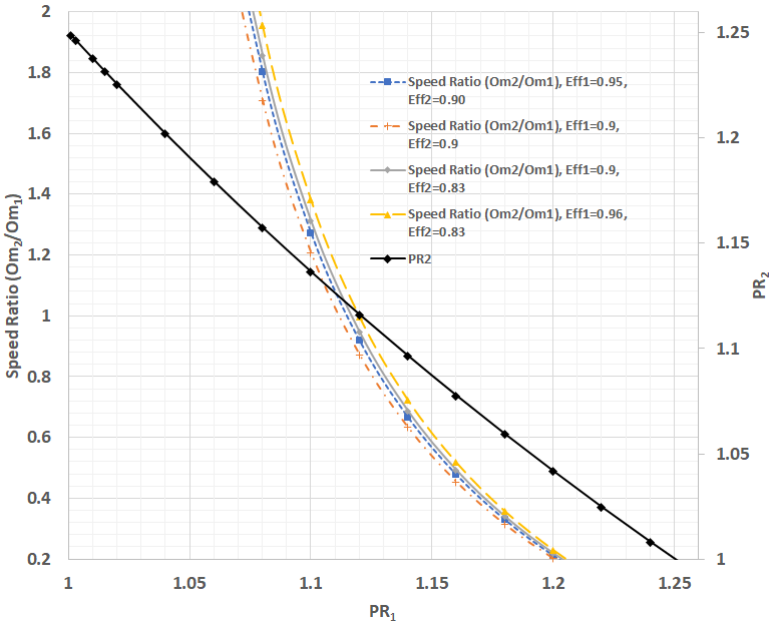

Figure 5: Determination of speed and pressure ratios of counter-rotating fans.

III.3. Distortion Tolerance from Distributed Low Speed/Low Pressure Counter-Rotating Fans

Full-annulus multi-stage CFD models are created for the CRFs using Turbo R02.2018[17]. Since the URANS (Unsteady Reynolds Averaged Navier-Stokes) analysis is performed for the conceptual design, discussions in this studyr focus on how TURBO facilitates the design and provides a numerical assessment of the performance penalty resulting from the non-axisymmetric inlet profile. Thus, detailed CFD studies such as grid refinement studies are not addressed in the paper. Instead, the mechanism of how the low-speed, low-pressure fan, can tolerate the incoming distortions from BLI propulsion is investigated.

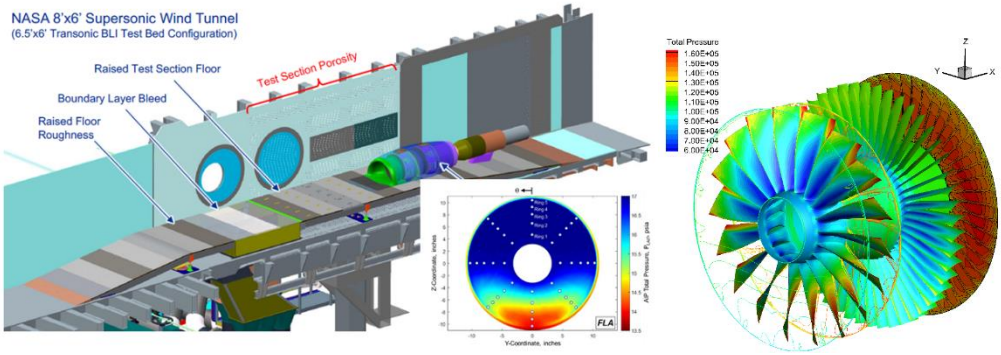

Figure 6: BLI2DTF test set-up in NASA's 8'x6' Supersonic Wind Tunnel (Left) and CFD analysis model (Right), Example to Investigate the Flow Physics for Fan Stage Efficiency Penalty due to Distortion at the Inlet of Boundary Layer Propulsion Systems. [9, 24]

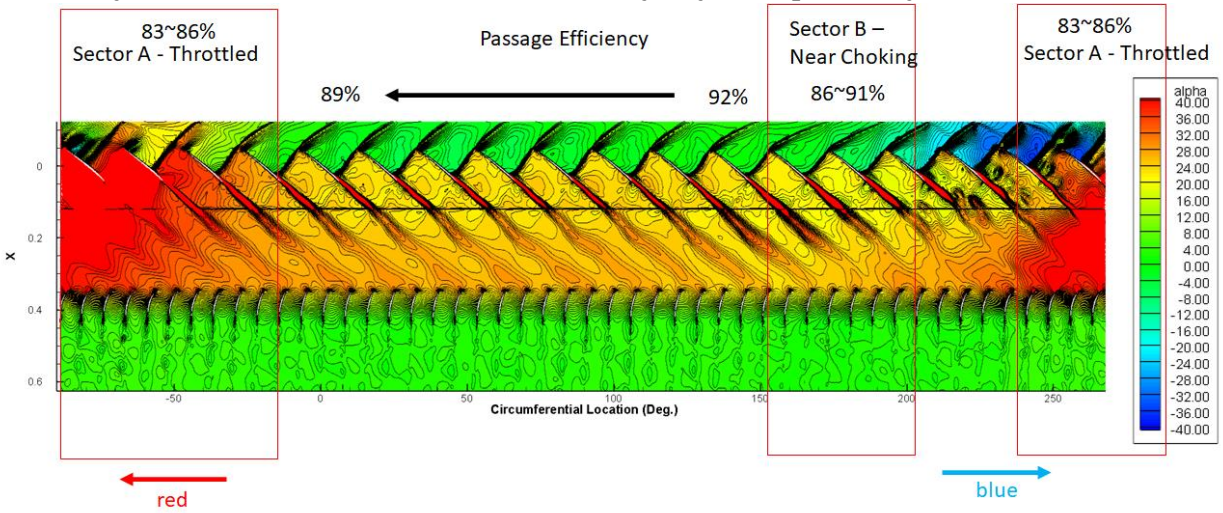

Figure 7: Swirl distribution in blade to blade view along the 90%Spanwise location of BLI2DTF fan stage at ADP. [24]

Here, the BLI2DTF CFD results, as shown in Figs.6, are used as an example to explain the impact of the non-axisymmetric inlet profile from boundary layer ingestion on the fan efficiency. The condition of the results is at the ADP point (i.e., FSPR=1.31, MFRc=47.8kg/sec) with a non-axisymmetric inlet profile. [9] Even though the case is analyzed at the design condition, the peak stage efficiency barely reaches 87%, while the conventional clean inlet flow fan can easily exceed 93% polytropic efficiency for the same operating conditions [24]. Figure 7 shows the full annulus swirl contour in a blade-to-blade section at 90%span location of the rotor. It indicates that as the inlet profile is circumferentially non-axisymmetric, the operating conditions that individual passage experiences are significantly different from each other. Thus, the passages at sector A that pass the low momentum flow profile region are under near stall condition, while the passages at sector B passes high momentum area with negative flow incidence angles,

consequently choked. Hence, each passage of the rotor will operate in quite different conditions temporally as well as spatially. As a result, the BLI2DTF fan incurs efficiency degradation per passage and results in low fan efficiency. Given what has been observed in this example, the SUSAN's TeDP systems need to be desensitized in terms of operability to maintain good performance, and an effective method to desensitize the fan performance for the operating condition is to design the fan at a relatively lower rotational speed than the conventional fan designs.

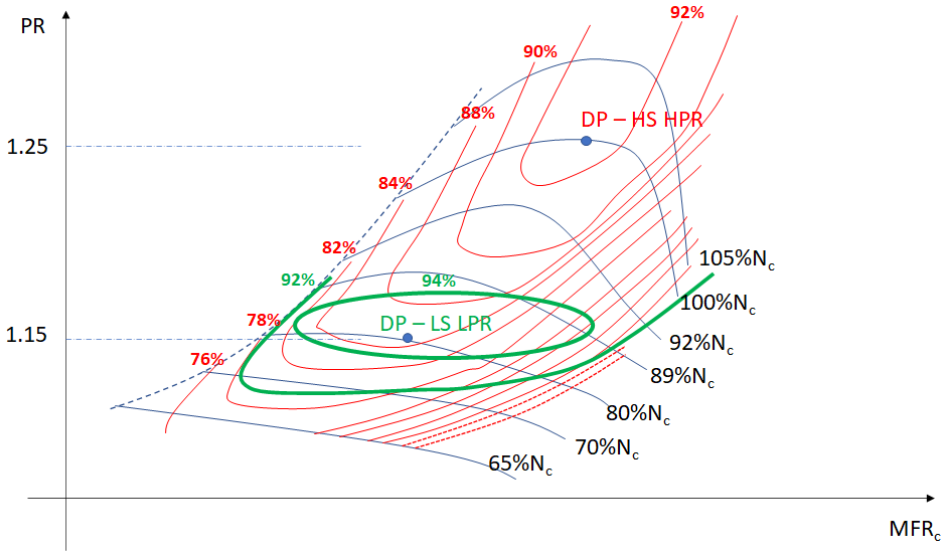

Figure 8: Illustration of the Comparison of Performance Characteristics between High-Speed High-Pressure Ratio and Low-Speed Low-Pressure Ratio Rotors.

An illustration of a high transonic fan map with a design pressure ratio at PR=1.25 is presented in Fig. 8. The comparison with a low-speed low-pressure fan designed at PR=1.15 is also depicted. The design point for a high-speed, high-pressure fan is denoted by 'DP-HS-HPR,' and red contours represent the efficiency. On the other hand, the design point of the low-speed low-pressure ratio one is denoted by 'DP-LS-LPR,' and its efficiency contours are plotted in green color. If the design point is set at the high-speed regime where blade tip Mach number is supersonic at about M_{tip}=1.2, the fan stage can achieve very high efficiency at the design point, but the threshold of the good efficiency is narrowed, and the passage performance is susceptible to the inlet corrected mass flow rate condition.

On the other hand, the low tip Mach number regime below M_{tip}=0.75, the peak efficiency points cover a wide range of inlet corrected mass flow rate conditions. Thus, the pressure ratio of the fan stage is also desensitized for the operating conditions. Of course, a low rotational speed for the same fan diameter will result in a relatively lower fan pressure ratio. However, counter-rotating fans with two multiplying and complimentary rows can reach the target pressure ratio and meet the thrust requirement. In addition, the CRFs propulsion system does not need OGV and outperforms the single-stage fan-OGV configuration.

A CFD model with the baseline design of the counter-rotating fans is analyzed for URANS, and the fan map of the propulsor for the design speed is plotted in Fig. 9. As can be seen in the speed lines of the front /rear rotors and the stage, the aerodynamic reaction of the fan stage is desensitized for the operating conditions. Both the front and rear rotors show high sustainability with almost constant performance over the whole speed line, and the stage pressure ratio is maintained consistently near the design target. It is also notable that the adiabatic efficiency of the stage is maintained at about 93% throughout the whole operating conditions. The low-pressure ratio due to splitting the total aerodynamic load onto the two rotors enables high efficiency on each blade row, and the low rotational speed allows good operability over a wide range of conditions along the speed line. The total pressure contours from two different conditions on the same

speed line are compared in Figs. 9. The contours from the two conditions look very similar except that the peak level is slightly higher at the near stall point. The similarity of the contours from the near-stall and near-choking conditions proves the rotors' insensitivity to a significant incidence swing at the leading edge.

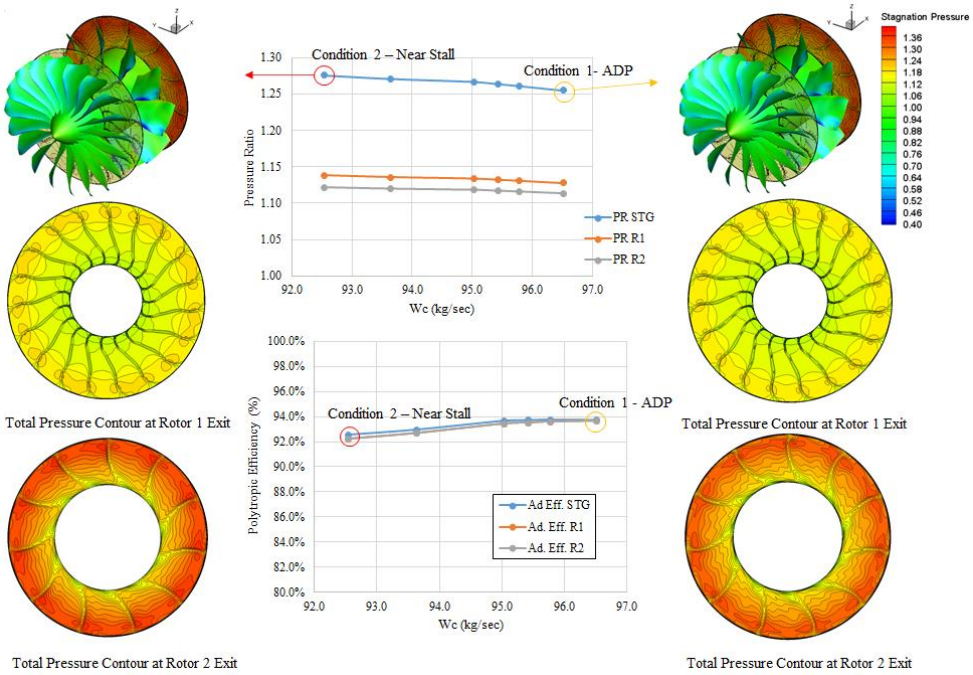

Figure 9: Performance Characteristics of Low-Speed Low-Pressure Ratio Counter Rotating Fans.

Figures 10 show the Mach number contours in the blade- to-blade view for the two conditions. Even though the near stall condition shows a high positive flow incidence angle, the width of the wake flow from the front rotor does not fundamentally grow compared with the near choking condition. A similar pattern is observed at the rear rotors so that the rotor performance is also insensitive to the incidence angles and the operating mass flow rate conditions. These characteristics of the counter-rotating fans mitigate the efficiency penalty due to the non-axisymmetric distortion significantly.

The inlet profile from the under-wing configuration in Fig. 3 is applied to the turbomachinery CFD model to evaluate the distortion penalty. The performance of a point with non-axisymmetric distortion is assessed and compared with the speed line of the clean inlet flow case. The offset is about 1%~1.5% depending on the reference condition. The degradation corresponds to the distortion affecting about five passages out of 19 for the front rotor. It is similar to the rear rotor as three passages out of 11 are involved, as shown in Figs. 12. Overall, 27% of the passages experience performance degradation. If the inlet distortion affects about 40% of the passages as seen in BLI2DTF case, the expected distortion penalty may be linearly projected to about 2.2%. Table 3 presents the shaft power requirement and thrust generation from the under-wing configuration. As the numbers consider the efficiency of the turbomachinery, the shaft-power requirement is raised by 6% compared with AD zone model-based analyses in the Table 2. Thus, the power saving is reduced to 7% with 92.7% stage efficiency of the counter rotating fans. BLI benefits from other concepts such as over-wing and trailing edge configurations are estimated via PAI CFD models and compared with each other in the following sub-chapter and finally an installation of mail-slots on 3-D wing is proposed as the conclusion of the chapter for the conceptual design of TDeP.

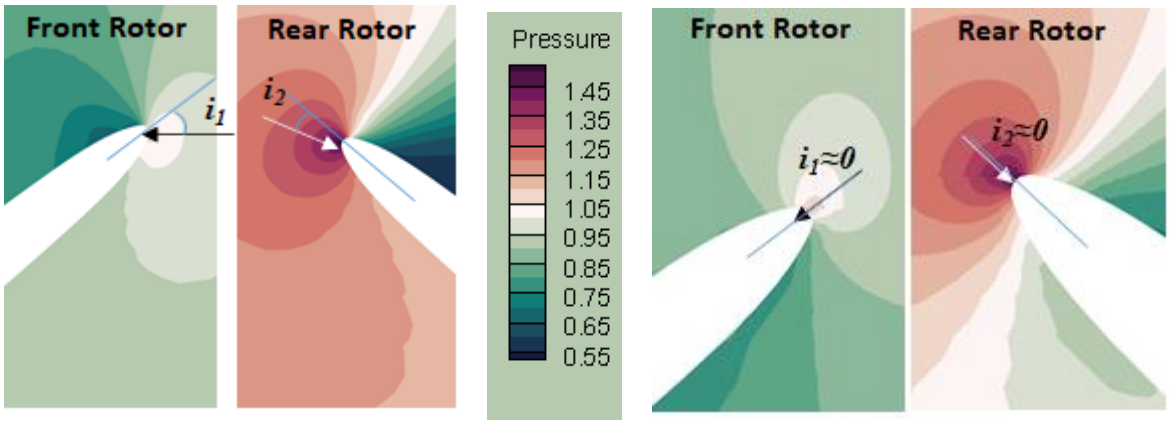

(a) Flow Incidence Angle for LE of Counter Rotating Fans (Left: Near Stall point MFR_c=92.5kg/sec, Right: Near Operating Line MFR_c=96.5kg/sec)

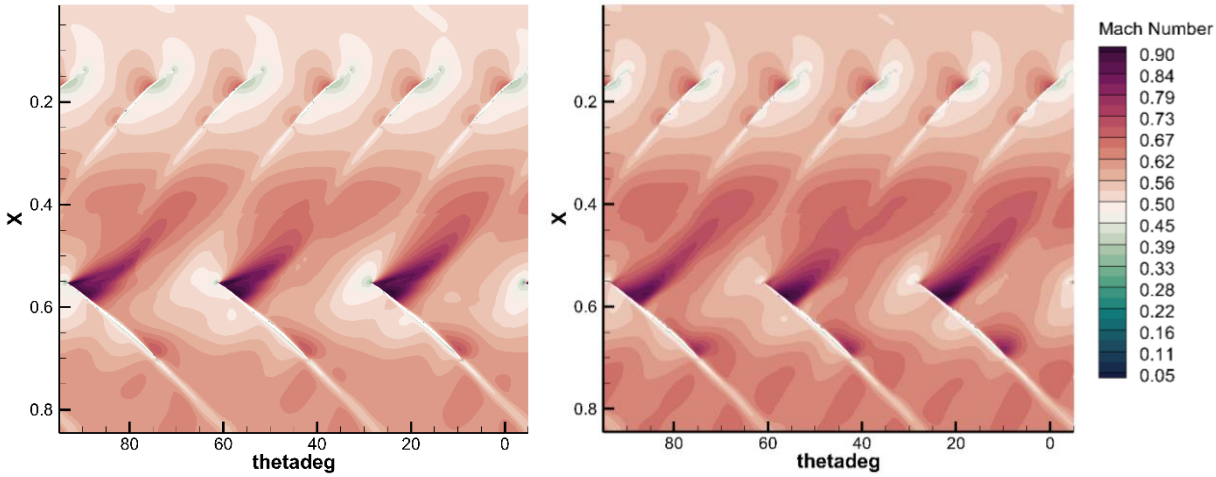

(b) Mach contours for Counter Rotating Fans (90%Span, Left: Near Stall point MFR_c=92.5kg/sec, Right: Near Operating Line MFR_c=96.5kg/sec)

Figure 10: Counter Rotating Propulsor Blade Design and Flow Pattern in Blade to Blade Views.

Table 3. Performance Summary of Counter-Rotating Fans for Under-Wing Configuration at ADP

No. of Engine Units	FSPR	Installation	Fan diameter [ft]	Shape Factor (H)	Iteration No. (PAI-CRF)
	1.25	Under-wing	2.41	1.14	04-01
16	MFR [kg/sec]	Shaft Pwr [MW]	Thrust Generation (kN)	Power Saving (%)	Polytropic Efficiency (%)
	30.3	0.52	2.08	7.1	92.7

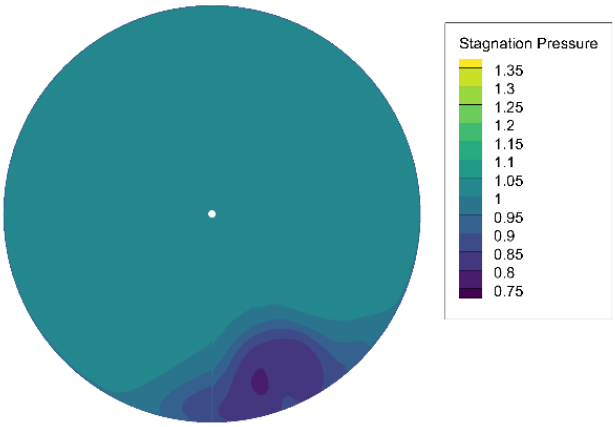

(a) Total Pressure Contour at the Inlet

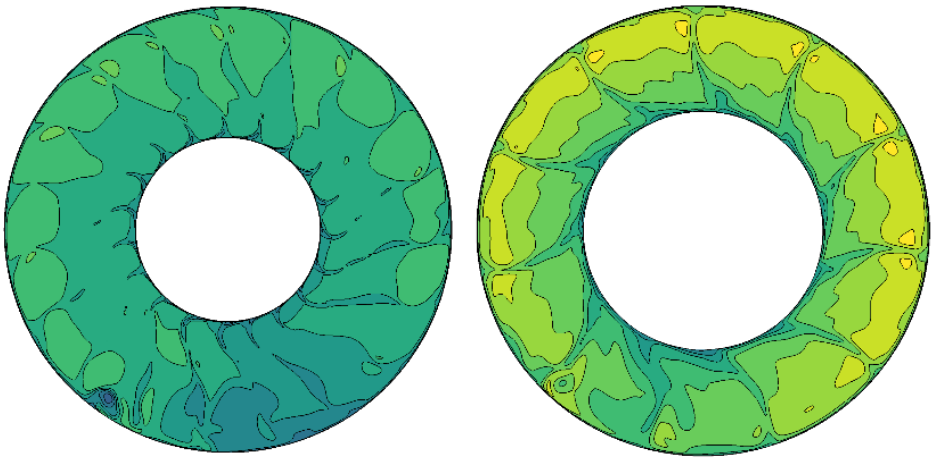

(b) Total Pressure Contour at the Rotor Exits (Left: Front Rotor, Right: Rear Rotor)

Figure 11: Migration of Distortion through the Counter Rotating Fan Stage.

III.4. Performance comparison of various concepts of installation.

The current iteration of the TeDP is originally designed for the installation of nacelle under the wing. However, two other concepts, such as over-wing and trailing edge installation, are also under consideration to find out the best trade-off between the airframe performance and BLI benefit, as shown in Figs. 12. [10, 15] The feasibility of the mechanical design for each concept is also a crucial factor to consider. Before deciding the concepts, each installation method's performance in terms of BLI benefits is compared and investigated as follows.

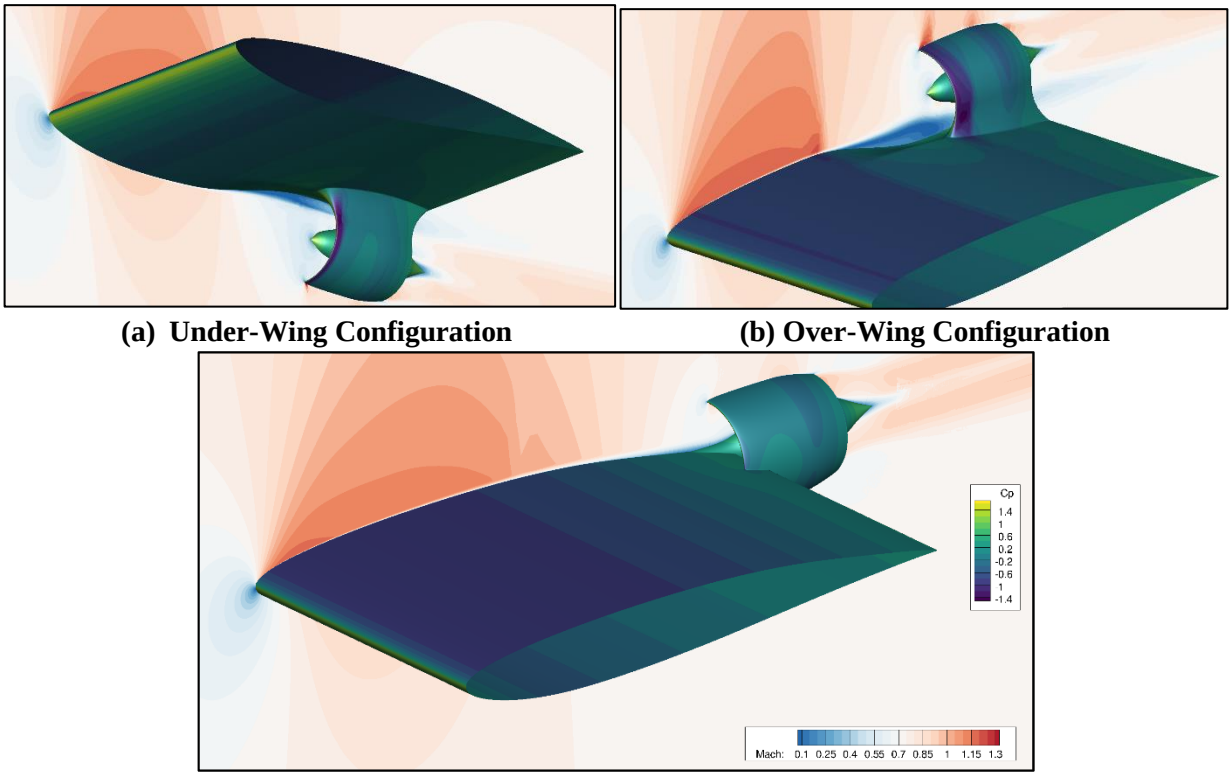

(a) Under-Wing Configuration **(b) Over-Wing Configuration**

(c) Trailing-Edge Configuration

Figure 12: Various Concepts of TeDP Installation [10, 15]

Figures 13 compare the inlet and exit profiles of the nacelles for the three concepts, including the underwing configuration. It could be simply found that the over-wing and trailing edge configurations ingest more boundary layer flow than the underwing configuration does. As mentioned earlier, the more low-momentum flow is ingested, the less ram drag is needed for the same amount of thrust generation. Thus, less shaft power is required, and more power saving through BLI propulsion is available, accordingly. [24] The power-saving and detailed performances of the configurations are compared in table 4. As the area of the low momentum region in the inlet profiles gets wider in the order of the under-wing, trailing edge, and over-wing configurations in Figs. 15, the ram drag is measured smaller accordingly. Thus, the power savings also grow in the same order. In addition, the mass flow rate requirements are lower for the cases with high power-saving and shape factors. However, the contours in Figs. 13 indicate that the low momentum flow region of the over-wing configuration shows a higher total pressure distortion in the circumferential direction than other concepts. In contrast, the trailing edge configuration is more uniform and concentric around the rotating axis of the fan stage, thus closer to axisymmetric profile. Hence, more detailed analyses with turbomachinery CFD for the additional two configurations will be needed to make sensible decision. The reports from the airframe design group indicate that the trailing edge configuration shows the least impact on the wing performance as the installation location moved much further

downstream of the wing.[15] In addition, the anti-shock body type installation of the rotor hub is intended to help the static pressure recovery along the airfoil. Thus, overall wing drag counts could be even reduced with the installed mail slot nacelle as well.[15]

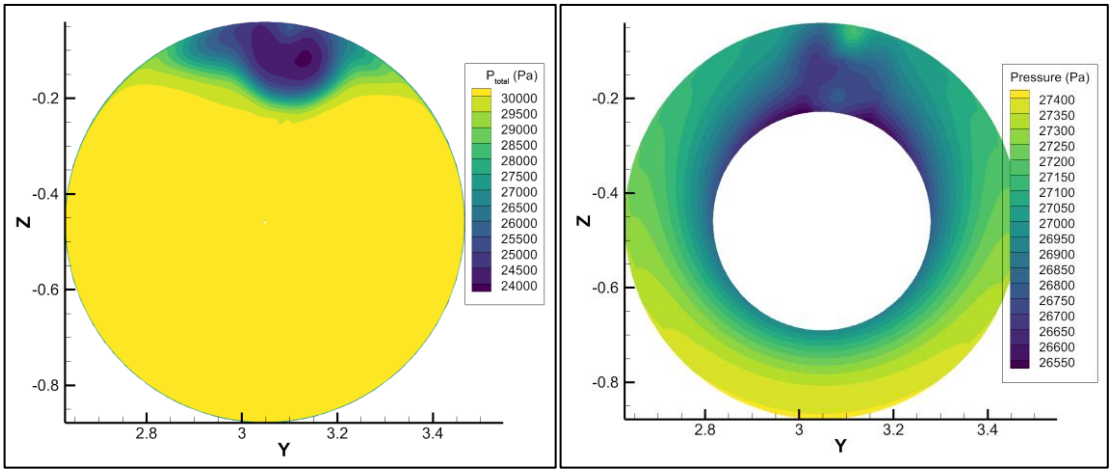

(a) Under-wing Configuration (L: Inlet, R: Exit)

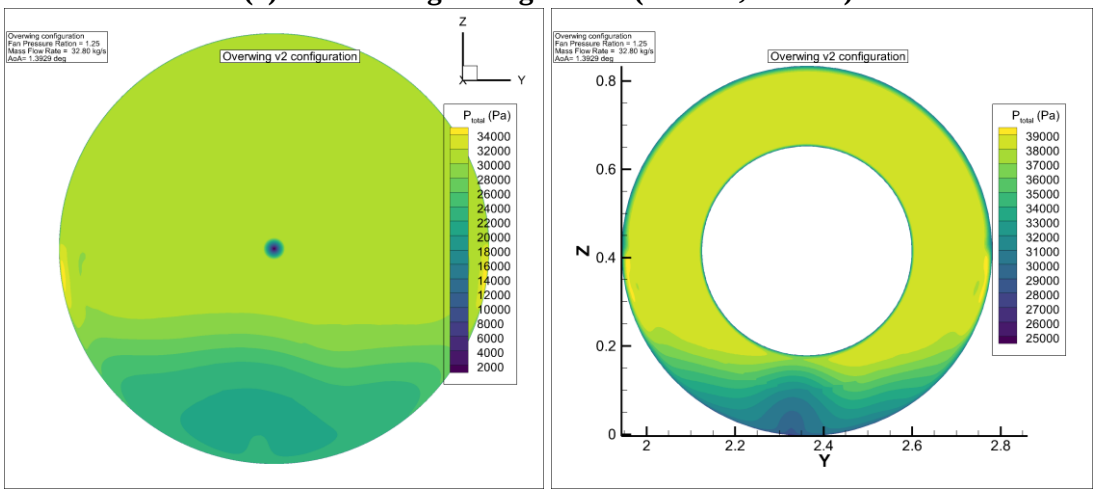

(b) Over-wing Configuration (L: Inlet, R: Exit)

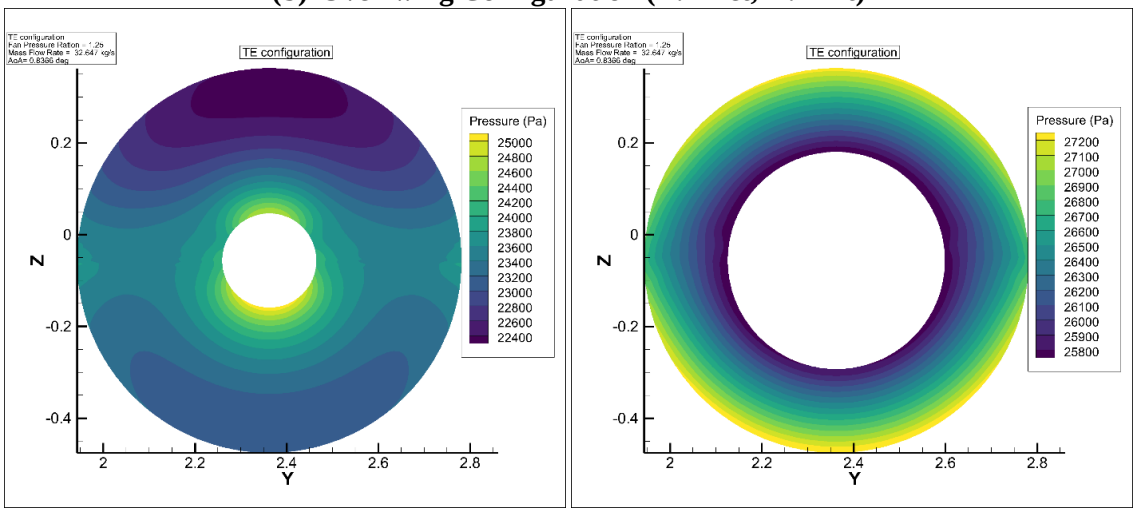

(c) Trailing Edge Configuration (L: Inlet, R: Exit)

Figure 13: Total Pressure Profiles at the Inlet and Exit of Various Concepts of TeDP Installation

Based on the observance from the external and internal flow analyses of the candidate prototypes, a novel concept of mail-slot nacelle installation that reduces the drag counts of a 3-D natural laminar flow wing is proposed as shown in Figs. 14. The enhanced static pressure recovery compensates for the drag increase due to the suction effect from the trailing edge mounted fan stages. In the current conceptual design, internal flow paths, including splitters between individual DeP units, are not modeled. However, the impact of the fan operation from the trailing edge for the wing aerodynamics can be clearly observed by propulsor modeling via actuator disks.[25] Furthermore, the thickness of the ingested boundary layer flow can be estimated before designing the flow path and the fan stage to adjust the nacelle sizing appropriately. As aforementioned, there is a significant interaction between the airframe and the nacelle. It is impossible to size the BLI engines from system design levels without incorporating the feedback from the high fidelity CFD models until enough database for the empiricism is accumulated. Consequently, a bottom-up type design process will be maintained throughout further detailed designs of sub-modules for the propulsion-airframe interaction (PAI) configuration.

Table 4. BLI Power-Saving for various installation methods of TeDP system at ADP

Methods	Under-wing	Over-wing	Trailing Edge
Shaft Power (MW)	0.49	0.41	0.46
MFR(kg/sec)	30.3	24.3	27.6
Shape Factor	1.14	1.24	1.22
FSPR	1.26	1.28	1.27
Power Saving (%)	12.2	26.9	17.4

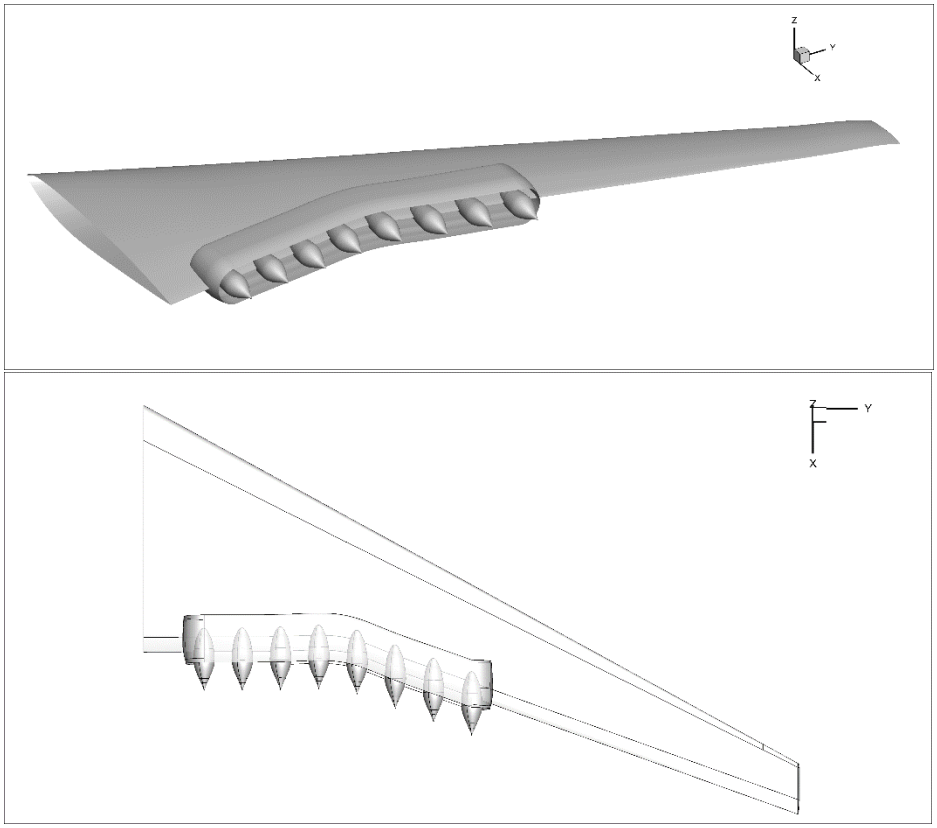

Figure 14: Conceptual Design of TeDP on 3D wing for 16 Propulsor Type. (Upper: Isometric View, Lower: Top View of Mail-Slot with Anti-Shock Body Type installation)

IV. SUSAN-TCT: Tail-Mounted TCT Propulsor

The BLI tail-cone thruster is mounted to the vertical tail in the rear, as shown in Fig. 15. It consists of an engine core for the power extraction, as illustrated in Fig. 2. Figure 15 depicts that the turbo-jet engine is strongly coupled with the airframe, and the trailing edge of the vertical tail is extended into the nacelle and aligned with the IGV (inlet guide vane) row. As above-mentioned, the thrust contribution of the tail-mounted engine is 35% of the total thrust requirement and reaches about 17.9kN at 37,000ft altitude for the top of the climb.[10] Here, the core generates about 6.5kN while the bypass takes 11.4kN, respectively.

Unlike the conventional turbo-jet engines, the tail-mounted TCT incurs a Type-II distortion [12] and the flow blockage from the vertical tail at the inlet. At a given target thrust from the system analysis, issues and tasks involved in the conceptual design are the fan sizing, inlet guided vane (IGV) to avert the distortion, appropriate bypass ratio, and nozzle designs. Thus, topics discussed in this section include the design processes and the resulting component-level design. For instance, the nacelle sizing is optimized for the flight missions, rotor design, bypass duct, flow-path, nozzle shapes, and the rest of the configurations associated with the IGVs. Each task will be addressed and analyzed accordingly as follows.

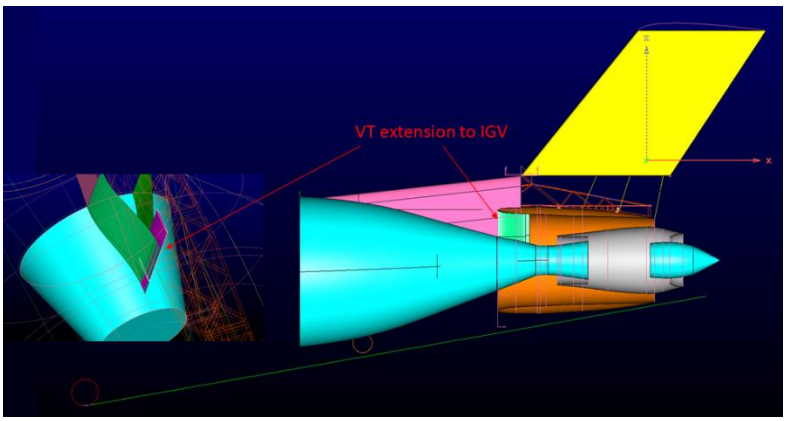

Figure 15: Overview of tail-mounted engine installation with the vertical tail.

1. Conceptual Design of Boundary Layer Ingesting Propulsor

The boundary layer ingesting propulsion creates additional difficulty in the analyses and prediction for the design. The characteristics of the captured flow by the inlet can hardly be represented by 1-D averaged numbers. Thus, the conventional system design methods using 0-D and 1-D models on the NPSS (Numerical Propulsion System Simulation) framework [20] will underpredict the inlet captured areas for the whole BLI engine and the core. [19] In addition, the shape factor of the boundary layer cannot be appropriately considered during the low fidelity model-based system design process. Thus, high-fidelity CFD analyses are indispensable even at the conceptual design stage of the engine to secure the required mass flow rate for the fan and core modules.

The initially sized nacelle and core inlet lines based on theoretic turbulent boundary layer profile (seventh power rule) were forwarded to airframe aerodynamic designers at NASA Ames Research Center, LAVA team for propulsion-airframe integration (PAI) CFD evaluations.[20] Again, LAVA applies a quasi-steady actuator zone engine model. Figures 16 show the flow-field around the airframe and the tail-mounted propulsion system from the PAI CFD analysis for initially sized nacelle and core inlets.[20]

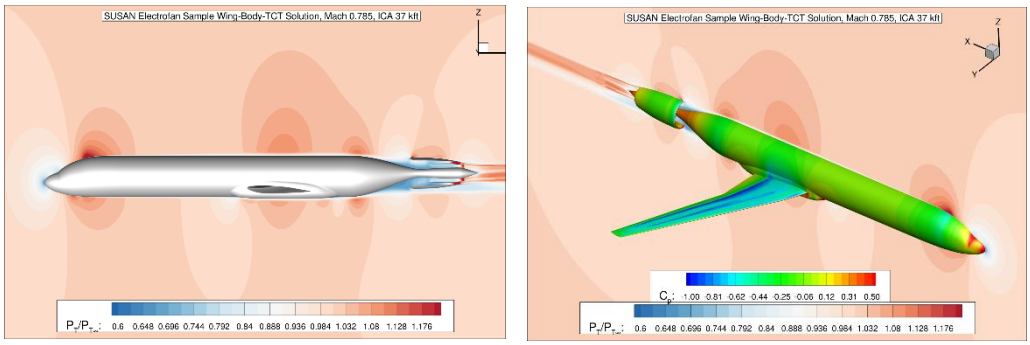

Figure 16: PAI simulation from LAVA [20]

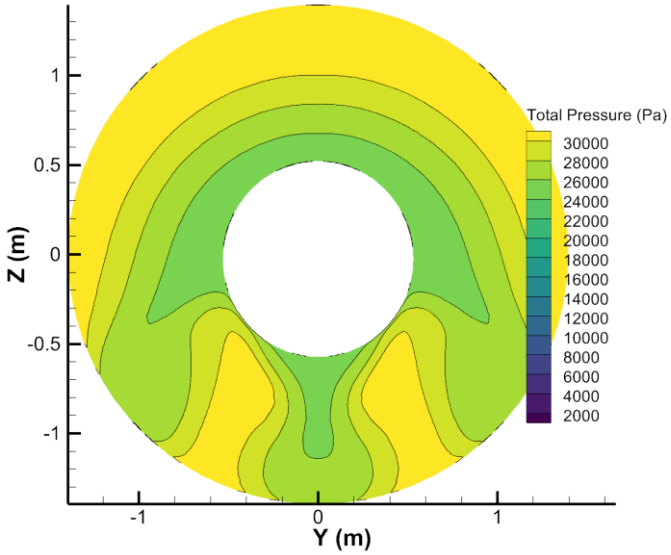

Figure 17: Inlet Profile from PAI simulation via LAVA[20]; PR=1.357, H=1.174, MFR=222.29kg/sec, Pressure Recovery 89.8%

Figure 17 shows the total pressure contour at the inlet of SUSAN's tail mounted engine with an actuator zone model. Meanwhile, three different thrust cases regarding the fan pressure ratio are chosen to capture the interactions of the airframe and propulsion systems, i.e., FSPR= 1.21, 1.285, and 1.357. Similarly, two initial core sizes are tested for various bypass ratios to understand how the distortion interacts with the geometric ratio between bypass and core duct areas.

The inlet captured area of the initial configuration is inevitably determined wider than the required for the clean inlet engine since the low momentum flow is ingested at the hub, as shown in Fig. 18. Figure 18 compares accumulated mass flow rate profiles (dashed lines) integrated from the hub to shroud along with the velocity profile for the case in Fig. 17. The velocity profiles (solid lines) for different fan pressure ratios are also compared for reference. The suction effect from the fan operation affects the captured area for the mass flow rate requirement. However, the variation among the BLI profiles is still much smaller than the difference from the uniform clean inlet profile (black-dashed line). As a result, the proposed radius of the inlet highlight is determined at 1.258 (m), while the radius for clean inlet flow nacelle is 0.973 (m). Thus, the nacelle area for the distorted inlet profile needs to be 2 times wider than conventional turbo-jet engines to capture same mass flow rate.

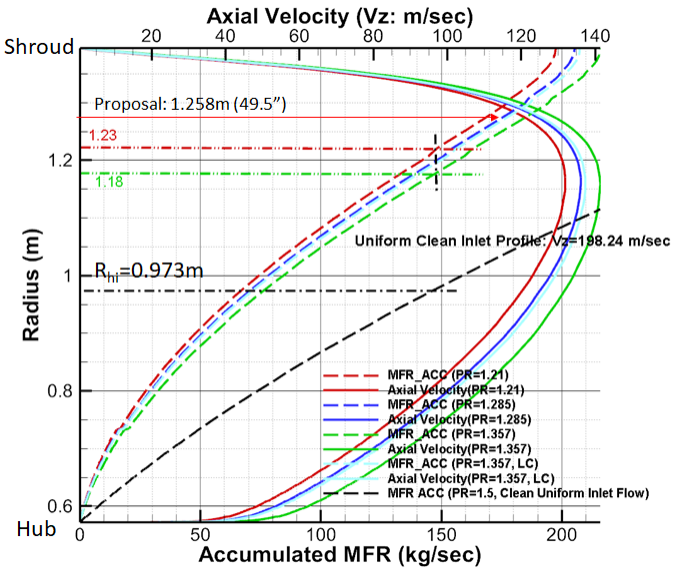

Figure 18: TCT inlet sizing determination from the perspective of PAI and through the parameter of accumulated mass flow rate. The Fan pressure ratio considered are 1.21(red), 1.285(blue), and 1.357(green).

2. Profile split into the bypass and core

The profile at the fan exit is split into the bypass and core ducts. Figures 19 depict the 2D profile at the highlight of the splitter. As the actuator disk zone adds energy to the airflow without turning, the circumferential mixing effect at the fan exit station could not be observed in the figure. However, the circumferentially averaged profile in Fig. 20 provides a reasonable estimation for the captured areas of both the bypass and core ducts. The radius of the splitter is initially determined at 0.8(m) based on bypass ratio (BPR) from baseline NPSS data. [19] The axial velocity profile (solid lines) below R=0.8 (m) shows the profile into the core, and those above R=0.8(m) depict the profile into the bypass duct. The mass flow rate requirement for the core is 32.4 kg/sec (=71.38 lbm/sec) and 114.43 kg/sec (=252.27 lbm/sec) for the bypass duct (BPR= 3.53). Thus, the integrated mass flow profile (red arrows) indicates that the splitter radius is required to be R=0.67 (m) while that of the clean inlet flow profile is good for a much smaller size at R=0.57 (m). The captured area of the core inlet is 1.8 times wider than that of the conventional turbo-jet engine. A notable change in the profile shape is that the profile progresses flatter shape into the core duct. The blockage from the splitter slows down the flow at the shroud of the core duct and accelerates the flow at the hub relatively. The change provides a positive effect on the core performance. However, the 2-D profile in Fig. 19 indicates that the non-axisymmetric IGV design of the low-pressure compressor (LPC) is needed as the circumferential distortion is still observed in the fan exit profile.

3. Distortion tolerant fan (DTF) stage design

As mentioned earlier, wake flow from the airframe will not be circumferentially uniform once it is ingested into the nacelle. Both the pressure and swirl distortions will affect the fan stage performance significantly. The current fan design study estimates the efficiency penalty from the circumferential distortion compared with the axisymmetric distortions under full-annulus turbomachinery URANS CFD and performed the IGV and mapping design for non-axisymmetric inlet distortions. The target fan pressure ratio is set to 1.37. The test article is mainly designed for NASA's 11 ft wind-tunnel testing for studying BLI thrust generation, as shown in Figs. 21. It has a shorter-body airframe but is facilitated with a boundary layer thickener to match the BLI level similarly to the B737 aircraft scale for the inlet size of the tail-

mounted nacelle. The inlet profile is obtained from a loosely coupled PAI approach using the body-force model. A full annulus URANS CFD model is built for the design and performance assessments of the fan stage. Thus, the designed DTF and IGV configurations are scaled and applied to the SUSAN aircraft as baseline propulsor design.

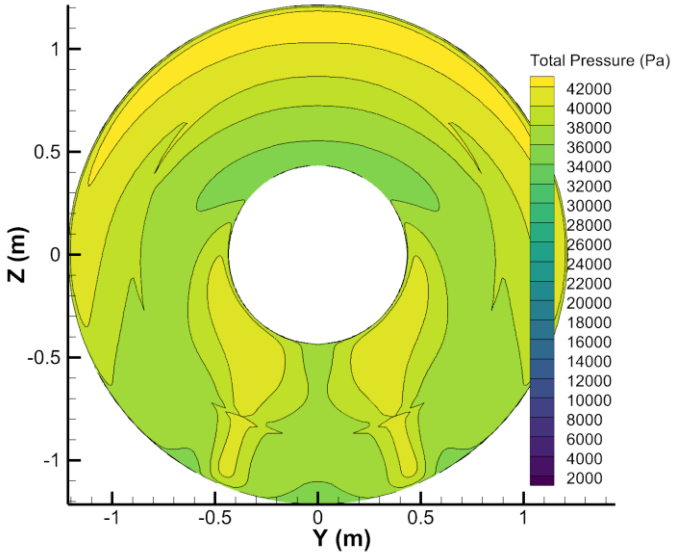

Figure 19: PAI simulation from LAVA (courtesy of Duensing et al.); PR=1.357, H=1.174, MFR=222.29kg/sec

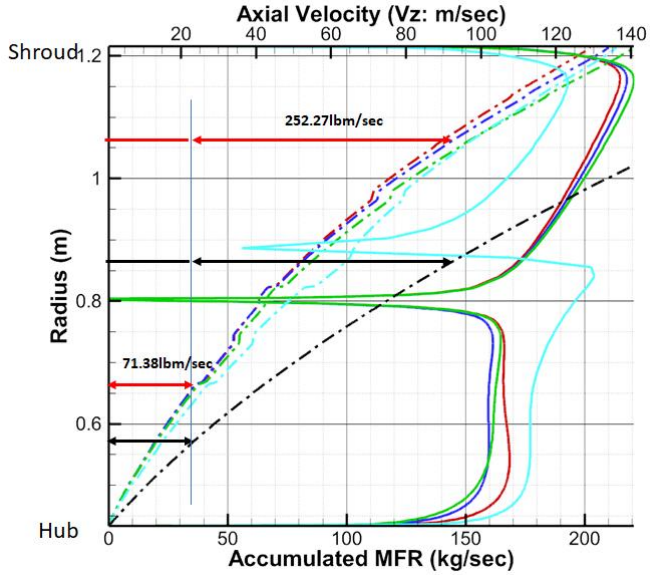

Figure 20: Core engine inlet sizing determination through the parameter of accumulated mass flow rate. Fan pressure ratios considered in the parametric study are 1.21(red), 1.285(blue), and 1.357(green).

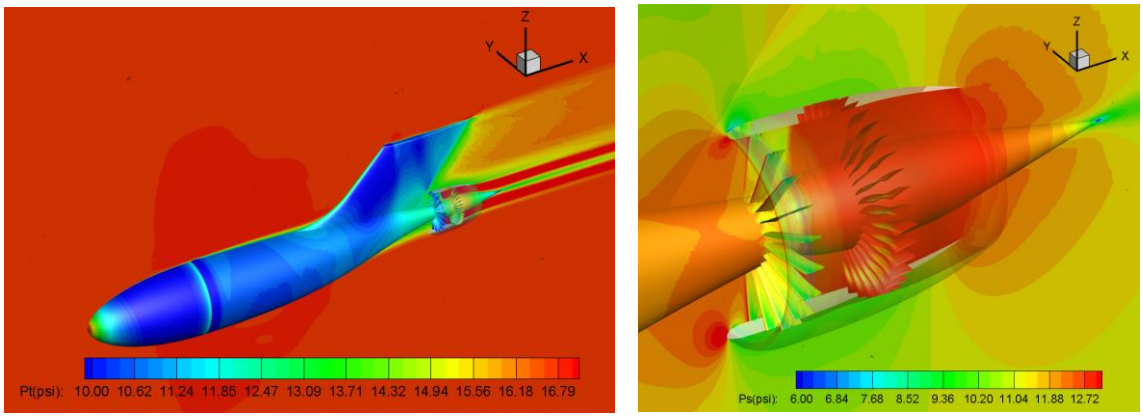

(a) **(b)**

Figure 21: PAI simulation for the Inlet Profile for the Fan Stage Design, (a) surface total pressure contours, (b) close-up view of the TCT fan stage of IGV, rotor, and OGV where body-force model models rotor.

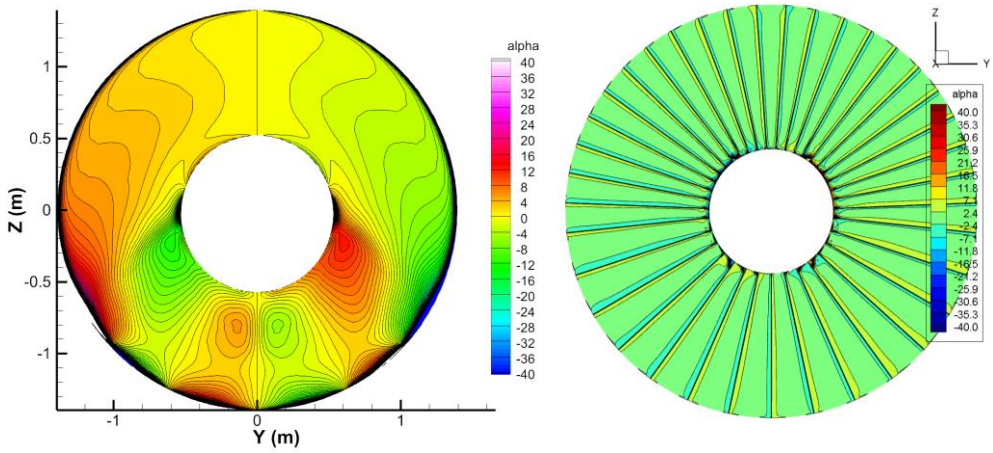

(a) **(b)**

Figure 22: Control of Swirl Distortion by using non-axisymmetric IGV and mapping designs as in (b) to mitigate the swirl distortion from inlet as in (a).

The ingested low momentum flows into tail mounted TCT include the wakes of the vertical tail and wings. In addition, the angle of attack during the flight causes upwash on the fuselage along with the rotor hub. These detrimental flow patterns from the wake ingestion cause significant non-axisymmetric swirl distortion, as shown in Fig. 22-(a). The fan performance will be significantly degraded because of the non-uniform incidence angles at the rotor leading edge per clock location. Thus, the current conceptual design considers adopting non-axisymmetric IGV methods to reduce the performance degradation from the swirl distortion. Figure 22-(b) shows the current iteration of a non-uniform IGV mapping and shows a remarkably efficient control of the inlet swirl at the fan face. Further details of the IGV design can be found in the ref. [26]

The fan stage is optimized for the Type II distortion through the propulsor design for STARC_ABL configuration.[22-23] The fan performance along the speed line is assessed with inlet profiles of SUSAN electro-fan aircraft in Fig. 23. Full annulus URANS CFD analyses are performed to predict the distortion penalty of the fan stage. Figures 24 present the two speed lines for a non-axisymmetric inlet profile from figure 22 and axisymmetric profile by taking a circumferential mass-weighted average of the 2D profile. The analyses are performed for standard air conditions at 12” scale fan size for the target pressure of SUSAN conceptual design.

The efficiency penalty due to the non-axisymmetric profile is about -2.2%, and the choking mass flow rate difference is about 2% less than the axisymmetric profile data. The points on each speed line are chosen at FPR=1.38 for a back-to-back comparison. As can be seen in the efficiency map (24-(b)), the peak adiabatic efficiency of the non-axisymmetric profile barely touches 88%, while the axisymmetric profile case is predicted over 90%. The reason for the degraded performance is found through the static pressure contours in Figs. 25 and 26. Figs. 25 depict the blade to blade view at 50%span location and Figs. 26 compare the contours at 90%span location of the rotor. As the contours visualize the flow pattern in all 18 passages of the rotor at an instance, the spatial variation of each rotor's flow pattern can be clearly observed. The passages in sector A in Fig. 25-(a) are choked as a strong normal shock is observed in the middle of the passage, while most passages in Fig. 25-(b) are free from shock loss. Thus, a significant variation of the efficiency is expected per passage for the non-axisymmetric inlet profile cases. This spatial variation of the flow pattern is more prominent in Figs. 26-(a) than the mid-span section. The passages in sector A are choked, those in the sector B are stalled, and only about 6~7 passages in sector C operate near the peak efficiency conditions. On the other hand, most passages in the axisymmetric profile case show a flow pattern of the near peak efficiency or slightly choked around the operating line as observed in Fig.26-(b).

V. Conclusion

Conceptual designs of the propulsion modules for the Susan electro-fan aircraft are presented. Furthermore, their performances, especially the power savings from boundary layer ingesting propulsions, are assessed through loosely coupled PAI and turbomachinery CFD models.

The non-axisymmetric profiles of the ingested flow into the nacelle prevent the simple 0-D and 1-D models from properly sizing propulsion systems. As a result, the current study started the bottom-up design process from high fidelity PAI CFD analyses instead of top-down from NPSS data. However, overall requirements for each module should still be based on the system-level analyses. Thus, a couple of critical parameters and specifications are drawn from the system-level design for the initial sizing, and the analysis results from PAI CFD are feedbacked to update the NPSS based design. Throughout this hybrid type design process by iterating bottom-up and top-down processes, initial conceptual designs for TeDP and TCT modules are developed.

The TeDP systems adopt sixteen distributed engines and share 2/3 of the total thrust requirement. Here, eight engine modules are installed on each wing and enclosed in a mail-slot type nacelle. Each unit requires about 0.56MW shaft power at the 37,000 ft altitude condition. By adopting BLI propulsion technology, the shaft power requirement can be reduced to 0.41~0.49MW levels depending on the configurations that correspond to about 13~23% of power saving with the ideal propulsor assumption. However, the ingested wake flow profile inherently has total pressure and swirl distortions that cause efficiency degradation of turbomachinery propulsors. Thus, low-speed low-pressure counter-rotating fans (CRFs) are adopted as part of the effort to minimize the deficiency. Its performance under the operating condition at ADP is assessed for the under-wing configuration. The power-saving is slightly degraded from 13% to 7% due to the distortion penalty, but the efficiency evaluated from CRFs for Type I distortion is still much lower than high-speed fans. The tip Mach number reaches about M_{tip}=1.2. The theoretical background of the mitigation of efficiency penalty using low-speed fans is discussed by explaining the concept's design process.

Regarding the TCT module, the reason why high fidelity PAI CFD should involve even in the system design process is discussed, and an example of the sizing of BLI engine and core ducts using CFD driven profiles. Integration of nacelle with a vertical tail of the aircraft and the role of IGVs in controlling the incoming swirl distortions are addressed. Furthermore, CFD analyses and the baseline fan stage performance are assessed to estimate the distortion penalty from Type II distortion from the fuselage.

Acknowledgement

The Convergent Aeronautics Solutions (CAS) Project, which is part of the Transformational Aeronautics Concepts Program (TACP) in the NASA Aeronautics Research Mission (ARMD) Directorate, sponsors this work. The authors would like to express special thanks to LAVA CFD team members – T. Chau., L. G. Machado, J. C. Duensing, and C. C. Kiris – at NASA Ames research center for their active collaboration via extensive analysis and development of various propulsion-airframe-integration models.

References

[1] Jansen, R. and Kiris, C. "Subsonic Single Aft Engine (SUSAN) Transport Aircraft Concept and Trade Space Exploration," AIAA SciTech Forum and Exposition, AIAA 2022, San Diego, CA, January 2022.
[2] Kim, H.D, Perry, A. T, and Ansell, P. J., "A Review of Distributed Electric Propulsion Concepts for Air Vehicle Technology," AIAA/IEEE Electric Aircraft Technologies Symposium, July 9-11, 2018, Cincinnati, Ohio https://doi.org/10.2514/6.2018-4998
[3] Lee, B.J., Liou, M-F, Celestina, M., To, W., "Benefit and Critical Factors for the Performance of the Boundary Layer Ingesting Propulsion," GT2020-15596, Turbomachinery Technical Conference and Exposition, GT2020, June 22-26, 2020, London, UK.
[4] Smith, L. H., "Wake Ingestion Propulsion Benefit," J. Propulsion and Power, Vol. 9, 74-82, 1993.
[5] Welstead, J. and Felder, J. L., "Conceptual Design of a Single-Aisle Turboelectric Commercial Transport with Fuselage Boundary Layer Ingestion," AIAA 2016-1027, 2016. https://doi.org/10.2514/6.2016-1027, URL.
[6] James L. Felder, Sydney L. Schnulo, Michael T. Tong, Jeffrey J. Berton, Robert P. Thacker, and William J. Haller "An Updated Assessment of Turboelectric Boundary Layer Ingestion Propulsion Applied to a Single-Aisle Commercial Transport," *AIAA SciTech Forum and Exposition*, AIAA 2022, San Diego, CA, January 2022.
[7] Florea, R., Voytovych, D., Tillman, T. G., Stucky, M., Shabbir, A., Sharma, O., and Arend, D. "Aerodynamic Analysis of a Boundary-Layer-Ingesting Distortion-Tolerant Fan," GT2013-94656, ASME Turbo Expo 2013: Turbine Technical Conference and Exposition, June 2013. DOI:10.1115
[8] Ochs, S. S., Tillman, G., Joo, J., and Voytovych, D. M., "Computational Fluid Dynamics-Based Analysis of Boundary Layer Ingesting Propulsion," *Journal of Propulsion and Power*, Vol. 33, No. 2, 2017, pp. 522–530. https://doi.org/10.2514/1.B36069, URL https://doi.org/10.2514/1.B36069.
[9] D. J. Arend, J. D. Wolter, S. M. Hirt, A. J. Provenza, J. A. Gazzaniga, W. T. cousins, L. W. Hardin and O. P. Sharma, "Experimental Evaluation of an Embedded Boundary Layer Ingesting Propulsor for High Efficient Subsonic Cruise Aircraft," AIAA 2019-5041.
[10] Chau, T., Kenway, G. K. W., and Kiris, C. "Conceptual Exploration of Aircraft Configurations for the SUSAN Electrofan," *AIAA SciTech Forum and Exposition*, AIAA 2022, San Diego, CA, January 2022.
[11] Lee, B.J., Liou, M.-F. and Celestina, M. L., "Conceptual Design of a Counter-Rotating Fan System for Distributed Boundary Layer Ingesting Propulsion," ISABE 2019 -2019-24285, Sep. 25-27, Canberra, Australia.
[12] Celestina, M. L. and Long-Davis, M. J., "Large-Scale Boundary Layer Ingesting Propulsor Research," ISABE 2019 -2019-24264, Sep. 25-27, Canberra, Australia.
[13] Aungier, R.H. "Axial-Flow Compressors: A Strategy for Aerodynamic Design and Analysis," ISBN 978-0791801925.
[14] Lee, B.J., Liou, M.-F. and Kim, H., "Aerodynamic Conceptual Design of Boundary Layer Ingestion Propulsor Systems: Hybrid Wingbody Aircraft with Propulsion-Airframe-Integration," AIAA2018-3954, 2018.

[15] Machado, L., Chau, T., Kenway, G. K. W., Duensing, J. C. and Kiris, C. “High Fidelity Computational Analysis and Optimization of the SUSAN Electrofan Concept,” *AIAA SciTech Forum and Exposition*, AIAA 2022, San Diego, CA, January 2022.
[16] Kiris, C. C., Barad, M. F., Housman, J. A., Sozer, E., Brehm, C., and Moini-Yekta, S., "The LAVA Computational Fluid Dynamics Solver," AIAA 2014-0070, 52nd AIAA Aerospace Sciences Meeting, National Harbor, MA, Jan. 13-17, 2014. https://doi.org/10.2514/6.2014-0070
[17] *A Parallel Flow Solver for Unsteady Multiple Blade Row Turbomachinery Simulations*, Turbo Expo: Power for Land, Sea, and Air, Vol. Volume 1: Aircraft Engine; Marine; Turbomachinery; Microturbines and Small Turbomachinery, 2001. https://doi.org/10.1115/2001-GT-0348
[18] Lynde, M. N., Campbell, R. L., Hiller, B. R., “A Design Exploration of Natural Laminar Flow Applications for the SUSAN Electrofan Concept,” *AIAA SciTech Forum and Exposition*, San Diego, California, U.S.A., 2022.
[19] Arman M, Jeff C, Chris M, and Julia S, “Tail-mounted engine Architecture and Design for the Subsonic Single Aft Engine Electrofan Aircraft,” *AIAA SciTech Forum and Exposition*, AIAA 2022, San Diego, CA, January 2022.
[20] Duensing, J., “High Fidelity Computational Analysis and Optimization of the SUSAN Electrofan Concept,” *AIAA SciTech Forum and Exposition*, AIAA 2022, San Diego, CA, January 2022.
[21] NPSS, Numerical Propulsion System Simulation, NASA: Consortium Software Package, Version 2.6, 2013.
[22] B. Lee, M. Liou and M. Liou, “Aerodynamic Conceptual Design of a Tail-Cone Thruster System Under Axi-symmetric Inlet Distortion,” GT2018-75861, ASME Turbo Expo, IGTI, Oslo, Norway, 11-15, Jun., 2018.
[23] Lee, B. and Liou, M.-F., “Aerodynamic Design and Optimization of Fan Stage for Boundary Layer Ingestion Propulsion System,” ICCFD10-091, 10th International Conference on Computational Fluid Dynamics (ICCFD10), Barcelona, Spain, July 9-13, 2018.
[24] B. Lee, M-F. Liou, M. Celestina, and W. To, “Benefit and Critical Factors for the Performance of the Boundary Layer Ingesting Propulsion,”, Proceedings of the ASME Turbo Expo 2020: Turbomachinery Technical Conference and Exposition GT2020-15596
[25] Robert T. Biedron, Jan-Renene Carlson, Joseph M. Derlaga, Peter A. Gnoo, Dana P. Hammond, William T. Jones, Bil Kleb, Elizabeth M. Lee-Rausch, Eric J. Nielsen, Michael A. Park, Christopher L. Rumsey, James L. Thomas, Kyle B. Thompson, and William A. Wood, “FUN3D Manual: 13.6,” NASA TM 2019-220416
[26] Lee, B. and Stephens, J., “Mitigation of Swirl Distortion using Inlet Guide Vane for Boundary Layer Ingesting Aft-Mounted Propulsor,” GT2022-83397, Proceedings of the ASME Turbo Expo 2022: Turbomachinery Technical Conference and Exposition, Rotterdam, Netherlands, June 13-17, 2022.

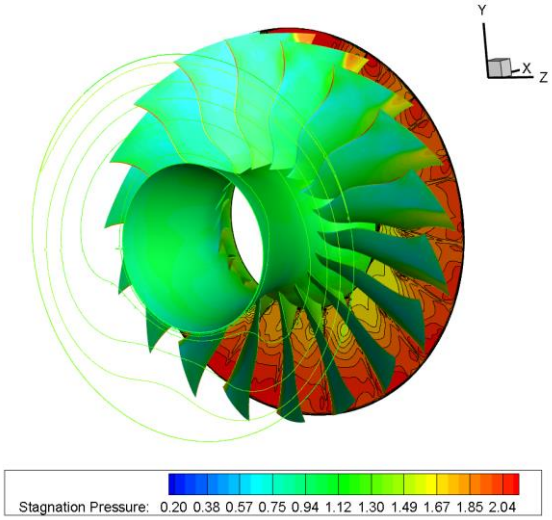

Figure 23: Full annulus URANS CFD for Fan Conceptual Design (Total Pressure Contour throughout the fan stage)

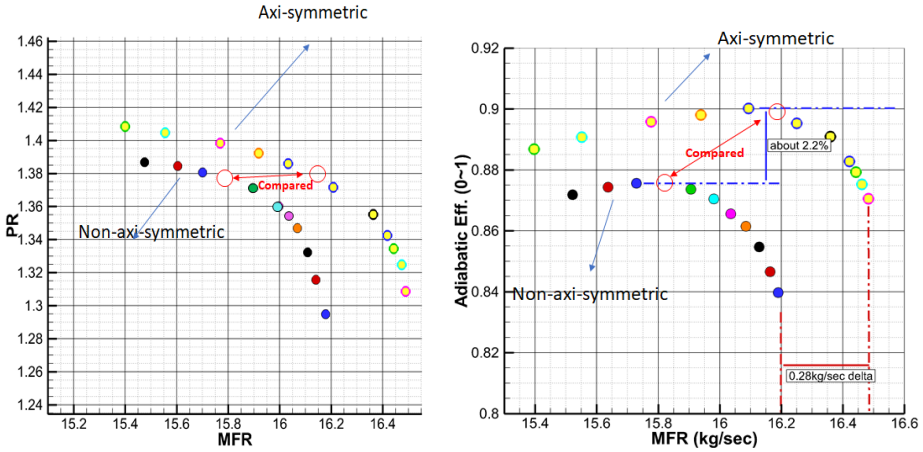

Figure 24: Comparison of Fan Performance between axi- and non-axisymmetric inlet profiles

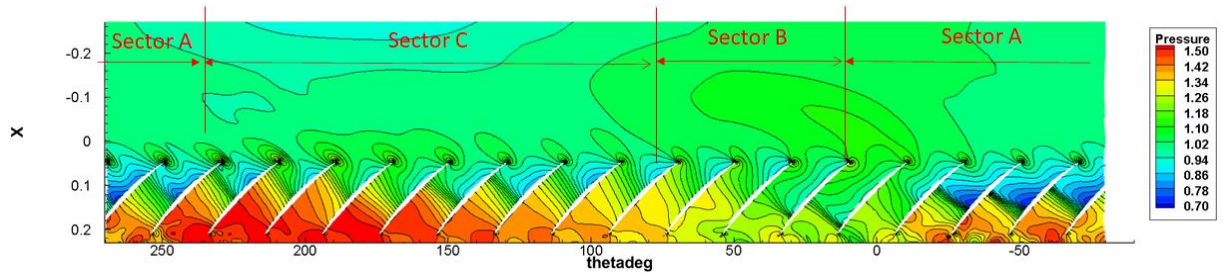

(a) Non-axisymmetric inlet profile

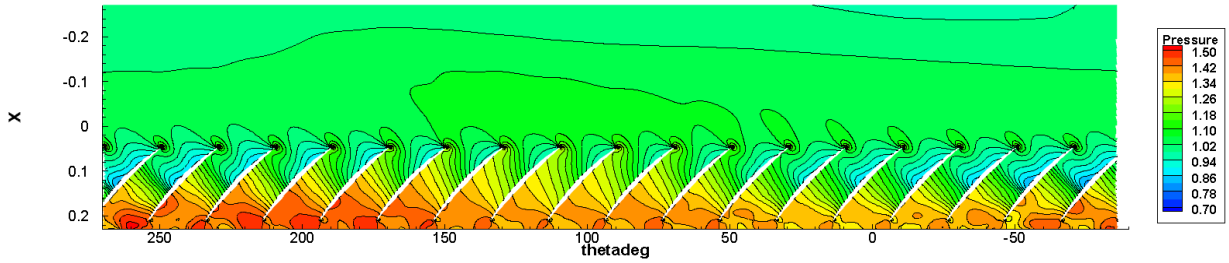

(b) Axisymmetric inlet profile

Figure 25: Comparison of Fan Performance between axi- and non-axisymmetric inlet profiles (blade to blade view, static pressure contours at 50%span)

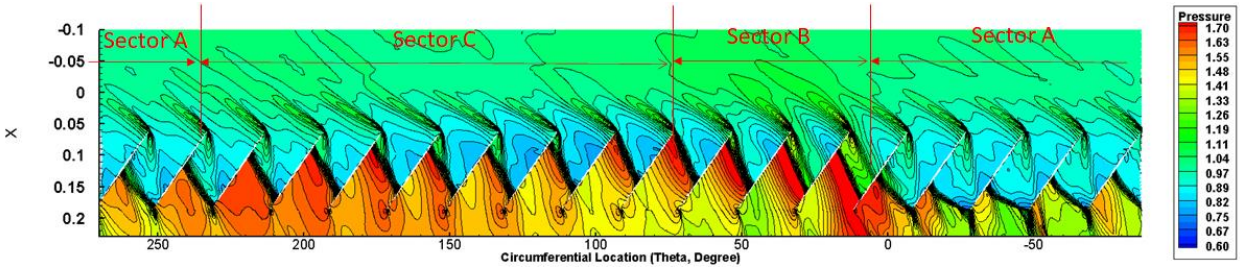

(a) Non-axisymmetric inlet profile

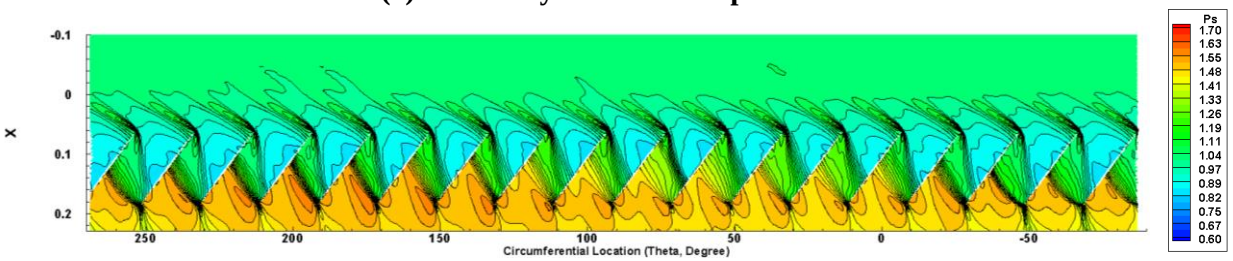

(b) Axisymmetric inlet profile

Figure 26: Comparison of Fan Performance between axi- and non-axisymmetric inlet profiles (blade to blade view, static pressure contours at 90%span)